JGR Oceans

Key Points:

- The Earth's rotation disintegrates the coherent wave packets and suppresses nonlinear oblique wave resonance
- The combined effect of topography and rotation modulates the birth and development of Mach stem
- This combined effect alters the post-interaction waveforms and leads to the emergence of a nascent undular bore

Correspondence to:
C. Yuan and Z. Wang,
yuanchunxin@ouc.edu.cn;
zwang@imech.ac.cn

Author Contributions:
Conceptualization: Chunxin Yuan, Zhan Wang
Formal analysis: Longxiang Pan
Funding acquisition: Chunxin Yuan, Zhan Wang
Investigation: Longxiang Pan
Methodology: Chunxin Yuan, Zhan Wang
Software: Chunxin Yuan, Longxiang Pan, Zhen Gao
Supervision: Chunxin Yuan, Zhan Wang
Validation: Longxiang Pan, Zhen Gao
Visualization: Chunxin Yuan, Longxiang Pan
Writing – original draft: Chunxin Yuan, Zhen Gao
Writing – review & editing: Chunxin Yuan, Zhen Gao, Zhan Wang

Combined Effect of Topography and Rotation on Oblique Internal Solitary Wave-Wave Interactions

Chunxin Yuan[1] , Longxiang Pan[1], Zhen Gao[1] , and Zhan Wang[2,3]

[1]School of Mathematical Sciences, Ocean University of China, Qingdao, PR China, [2]Institute of Mechanics, Chinese Academy of Sciences, Beijing, PR China, [3]School of Engineering Science, University of Chinese Academy of Sciences, Beijing, PR China

Abstract Oblique interactions between internal solitary waves (ISWs) in the ocean have been frequently recorded by satellite images, nonetheless, only a limited number of studies concentrate on these phenomena, which found that both the Earth's rotation and varying topography are important factors for the underlining wave dynamics. However, the effects of rotation at different latitudes and furthermore, their combined effects with the shoaling topography are still unclear. Thus, the aim of this paper is to investigate these combined effects on oblique ISW wave-wave interactions. Referring to observed obliquely interacting patterns, three scenarios initiated by two ISWs posing a V shape are explored using the variable-coefficient Kadomtsev-Petviashvili (KP) equation under the circumstance of continuous stratification and idealized shoaling topography. In all three experiments, rotation alone disintegrates the coherent waveforms and suppresses the emergence of a Mach stem (a wave generated at the interaction zone, characterized by the maximum of four-fold initial waves). When shoaling topography is also included, which increases the nonlinearity leading to a competition with dispersion induced by rotation, and the result is a magnification of wave amplitudes and emergence of additional trailing waves. The combined effect of these two factors modulates the birth and subsequent development of the Mach stem, alters the post-interaction patterns and determines the emergence of a nascent KdV-like undular bore, which plausibly explains the discrepancies between previous theoretical results (when the combined effect is not considered) and the measured horizontal surface signatures for ISW wave-wave interactions.

Plain Language Summary Internal solitary waves (ISWs) are large-amplitude internal waves featuring a robust hump shape and they are ubiquitous in the World's oceans. ISWs originating from different sources can propagate long distances in different directions, creating a high possibility for oblique interactions, which, indeed, have been frequently observed in satellite images. However, these three-dimensional phenomena are rarely studied, partly owing to the difficulty of collecting in situ data with appropriate spatial and temporal coverage. One of the remarkable features of wave resonance between oblique ISWs is the Mach stem wave which is characterized by an up to four-fold amplitude enhancement. Nevertheless, the combined effect of shoaling topography and Earth's rotation on oblique ISW wave-wave interactions is still unclear. In this paper, it is found that the post-interaction waveforms, the birth and development of the Mach stem, and the emergence of nascent wave packets akin to undular bores are influenced by this combined effect.

1. Introduction

Internal waves are ubiquitous in coastal waters, whose primary restoring force is a resultant force of gravity and buoyancy due to the ocean's stratification and the Coriolis force due to the Earth's rotation. Since the restoring force is weak, at order $\mathcal{O}(10^{-5} - 10^{-3})$ of gravity, two principal sources, the disturbance of the ocean's upper mixed layer by wind and barotropic tides passing over the topography, consequently trigger large-amplitude internal waves. Among them, internal solitary waves (ISWs) embodying a character of relatively stronger nonlinearity and larger amplitude have received extensive attention and research in the past decades (Guo & Chen, 2014).

Some studies found that the effect of the Earth's rotation on internal waves becomes significant when waves propagate over long distances and several periods of inertia, see Chao et al. (2006); Farmer et al. (2009); Li and Farmer (2011); Deng and Cai (2017); Helfrich and Ostrovsky (2022) for example, One of the earliest works examining the rotational effects on ISWs are based on a variation of the Korteweg-de Vries (KdV) equation, that is, the KdV equation with an additional rotation term, known as the Ostrovsky equation (Ostrovsky, 1978).

The incorporation of rotation amounts to exerting a long-wave dispersion on ISWs, whereby the existing balance between nonlinearity and dispersion is broken, and soliton-like waves decompose into weakly nonlinear inertial gravity waves and eventually a nonlinear coherent wave packet. Indeed, Grimshaw et al. (1998) and Grimshaw (2012) showed that no stable KdV solitary wave solutions exist in the rotational system using an asymptotic theoretical method and numerical simulations. Instead, the emergence of a wave packet was confirmed by Farmer et al. (2009) and Li and Farmer (2011) using in situ observational data, Grimshaw (2012) through theoretical analyses, Vlasenko et al. (2010); Zhang et al. (2011); Deng and Cai (2017) via numerical simulations of the Navier-Stokes equations, Grimshaw et al. (2013) laboratory experiments and Grimshaw et al. (2017) satellite images. Moreover, some relevant equations are also used to confirm this wave packet, for example, the weakly non-hydrostatic interfacial MCC equation (Helfrich, 2007), the higher order nonlinear Schrödinger equation (Grimshaw & Helfrich, 2008), and the forced Ostrovsky equation (Yuan et al., 2020). These wave packets can pass through each other or merge to form a longer wave packet when one wave packet catches up with another (Helfrich, 2007). Clearly, there are no stable "sech^2"-type solitary waves in the circumstance of the Earth's rotation; then one question arises: are there any stable solutions? The affirmative answer to this question was provided by Gilman et al. (1996), who constructed an approximate asymptotic solution to the Ostrovsky equation amounting to a solitary wave running adiabatically on a weak background long wave. More importantly, Grimshaw et al. (2014) examined the combined effect of the Earth's rotation and another important factor—shoaling topography—on the propagation of ISWs, and they demonstrated the presence of a secondary wave packet with the structure of a KdV-like undular bore, following the leading waves.

In the ocean, internal waves originating from different sources propagate along different directions, resulting in the possibility of oblique wave-wave interactions. In addition, the complex bathymetry and varying background leading to waves being reflected, refracted, or cut off into two branches (Jackson, 2004; Ramp et al., 2022) boost this possibility, among which catch-up and head-on collisions between solitary waves have been heavily studied and documented, see Su and Mirie (1980); Mirie and Su (1984); Cai and Xie (2010); Chen and Yeh (2014); Maderich et al. (2017); Zou et al. (2020); Yuan and Wang (2022) amongst many others. In contrast, oblique ISW wave-wave interactions have been sparsely investigated, partly done to the lack of observational data on this three-dimensional (3D) phenomenon, although Chen et al. (2011); Xue et al. (2014) examined this using satellite images. More importantly, distinguished from the studies solely using the horizontal snapshots from the orbital satellites, Wang and Pawlowicz (2012) conducted comprehensive analyses based on aerial photographs and the corresponding vertical thermohaline and current profiles. The numerical simulations on oblique ISW wave-wave interactions need a very subtle effort on model configuration, and they are generally time-consuming and expensive; one of the rare studies we have noted is Shimizu and Nakayama (2017), who investigated oblique ISW wave-wave interactions in the Andaman Sea based using high-resolution three-dimensional MITgcm simulations and extended Miles theory. In addition, the theoretical models applicable to this horizontally two-dimensional phenomena are sparse as well, among which, the Kadomtsev-Petviashvili (KP) equation (Grimshaw, 1981, 1985; Kadomtsev & Petviashvili, 1970), one of the variants of the KdV-type equations, is mainly used, see Yuan, Grimshaw, Johnson, and Wang (2018) for example.

The pioneering work investigating oblique ISW wave-wave interactions is by Miles (1977a); Miles (1977b), who found the Mach stem wave may appear in the interaction zone and classified the interaction as strong and weak according to the magnitude of the inclination angle. Recently, Kodama (2010); Yeh et al. (2010) modified and extended the applicability of the Miles theory to smaller incident angles, and Li et al. (2011) conducted laboratory water-tank experiments to verify these theories. It is noted that most of these previous researches explained the evolution of oblique ISW wave-wave interactions based on the recorded images where the emergence of a Mach stem born from interaction point is the main focus. Chakravarty and Kodama (2008); Chakravarty and Kodama (2009) found multi-soliton solutions to the KP equation, which embody the character of an arbitrary number of line solitons in the far field and complex interaction patterns in the near field. The most significant advantage of their method is that the KP equation's solutions delineating the observed ISW wave-wave patterns can be asymptotically constructed based on the amplitudes and angles of line solitons. Indeed, Chakravarty and Kodama (2013) applied this method to surface solitary waves and successfully constructed some analytic solutions from the photographed wave-wave interactions. Recently, Yuan, Grimshaw, Johnson, and Wang (2018) adopted this method to investigate the oblique interactions of internal solitary waves, in which the evolution regime of two initial waves in the form of a V shape is classified in one of six types, albeit two pairs of them can be transformed through an inversion of symmetry. More importantly, it illustrates that shoaling topography

significantly modulates the evolution regime. Yuan and Wang (2022) derived a bidirectional and isotropic modified Benney-Luke (mBL) equation and used it to examine the evolution of X-shaped ISW wave-wave interactions, where no conspicuous disparities between the KP equation (when inclination angles are smaller than 33°) were found and nonetheless, for the evolution of waves in the open ocean (waves are far from the computational boundaries), the mBL equation illustrates more closed results with the MITgcm model than the KP equation.

In aggregate, the combined effect of the Earth's rotation and shoaling topography on ISW wave-wave interactions is insufficiently studied, although Shimizu and Nakayama (2017) considered low latitude (9°N) with a small Coriolis parameter. The Earth's rotation amounts to exerting a long-wave dispersion on ISW wave-wave interactions, which competes with the extra nonlinearity induced by the shoaling topography, and expectedly, this competition would shape wave patterns and modulate wave amplitudes. Thus, in this paper, we examine the Earth's rotational effect and its combined effect with shoaling topography comprehensively by considering different Coriolis parameters imposed in distinguished evolution regimes. The governing equation is the variable-coefficient KP equation with an additional rotational term. Its mathematical expression and the corresponding numerical treatment are introduced in Section 2, together with the construction of the initial V-shaped solitary waves. Based on the frequently observed wave-wave interacting patterns in remote sensing images, three combinations of amplitudes and angles are selected to study the evolution scenarios under different rotational strength with (or without) shoaling topography in Section 3, where we highlight the modulation on the development of a Mach stem and the emergence of a nascent KdV-like undular bore. Finally, we conclude and discuss in Section 4.

2. Formulation

2.1. The Variable Coefficient KP Equation

In a rotating fluid, considering the varying background environment, the variable-coefficient KP (vKP) equation (Grimshaw, 1981, 1985) with the rotational term describing wave amplitude $\eta(x, y, t)$ can be expressed as

$$\left[\eta_t + c\eta_x + \frac{cQ_x}{2Q}\eta + \alpha\eta\eta_x + \beta\eta_{xxx}\right]_x + \frac{\gamma}{2}\eta_{yy} = \upsilon\eta, \tag{1}$$

where x, y, t are the respective horizontal spatial and temporal variables, and here the subscripts signify derivatives. The linear phase speed c, magnification factor Q, nonlinear coefficient α, dispersive coefficients β (x direction) and γ (y direction) and rotational coefficient υ are all obtained from the modal problem in the vertical z-direction pointing upward with $z = 0$ at the surface,

$$\begin{cases} \left[\rho_0(c - u_0)^2\phi_z\right]_z + \rho_0 N^2\phi = 0, & \text{for} -h < z < 0, \\ \phi = 0, & \text{at } z = 0 \text{ and } z = -h, \end{cases} \tag{2}$$

where the rigid lid assumption is invoked (see Yuan, Grimshaw, Johnson, and Chen (2018) for the scenario of the free surface). To illuminate the dynamics clearly, here the intrinsically two-dimensional topography is affirmed to vary solely in the x direction, $h = h(x)$; the background stratification is assumed to be horizontally uniform, $\rho_0 = \rho_0(z)$, whereby the buoyancy frequency $N^2 = -\rho_0/g\partial_z\rho_0$ (g is the acceleration due to gravity). Background current shear is given by ignored, $u_0(z) \equiv 0$. Equation 2 forms a classical Sturm-Liouville problem, with an infinite number of solution pairs (c_n, ϕ_n) corresponding to internal waves of mode $n = 1, 2, 3\cdots$. In this paper, only mode-1 waves are considered. A pseudo-spectral method based on Chebyshev interpolants is used to numerically obtain the first eigenvalue $c(x)$ and eigenvector $\phi(z; x)$ for mode-1 waves. Then all the coefficients are expressed as follows

$$\left.\begin{array}{l} Q = 2c^3 \int_{-h}^0 \rho_0\phi_z^2 \mathrm{d}z, \quad \alpha = \left(3c \int_{-h}^0 \rho_0\phi_z^3 \mathrm{d}z\right)\Big/\left(2 \int_{-h}^0 \rho_0\phi_z^2 \mathrm{d}z\right), \\ \beta = \left(c \int_{-h}^0 \rho_0\phi^2 \mathrm{d}z\right)\Big/\left(2 \int_{-h}^0 \rho_0\phi_z^2 \mathrm{d}z\right), \quad \gamma = c, \quad \upsilon = f^2/(2c), \end{array}\right\} \tag{3}$$

where the Coriolis parameter $f = 2\,\Omega\sin\varphi$ (Ω is the Earth's angular speed and φ is the latitude).

It is difficult to obtain analytical solutions to Equation 1 when the coefficients are not constants, as in this paper; thus, we have to resort to numerical methods. A transformation is introduced to increase the efficiency of numerical schemes,

$$\xi = Q^{1/2}\eta, \quad X = \int_{x_0}^{x} \frac{\mathrm{d}x}{c} - t, \quad T = \int_{x_0}^{x} \frac{\mathrm{d}x}{c}, \tag{4}$$

where x_0 is the initial location along x direction. After a straightforward calculation, Equation 1 is asymptotically equivalent to

$$[\xi_\tau + \mu\xi\xi_X + \xi_{XXX}]_X + \sigma\xi_{yy} = \kappa\xi, \tag{5}$$

where

$$\tau = \int_0^T \lambda(T')\mathrm{d}T', \quad \mu(y,\tau) = \frac{\alpha c^2}{\beta Q^{1/2}}, \quad \sigma(y,\tau) = \frac{\gamma c^4}{2\beta}, \quad \kappa(y,\tau) = \frac{\upsilon c^4}{\beta}, \quad \lambda = \beta/c^3. \tag{6}$$

2.2. Initial Waves

The vKP Equation 5 admits stable internal solitary waves in the absence of varying topography and the Earth's rotation, in which can the equation simplifies to

$$[\xi_\tau + \mu_0\xi\xi_X + \xi_{XXX}]_X + \sigma_0\xi_{yy} = 0, \tag{7}$$

where μ_0 and σ_0 are constants. It can further be written in the canonical form,

$$\left[4A_s + 6AA_\zeta + A_{\zeta\zeta\zeta}\right]_\zeta + 3A_{YY} = 0, \tag{8}$$

under the following transformation

$$\tau = Rs, \quad X = L\zeta, \quad y = LY, \quad \xi = PA, \tag{9}$$

where $R = L^3/4$, $L^2 = 3/\sigma_0$, and $P = 2\sigma_0/\mu_0$. Now the solution to this equation delineating internal solitary waves in any direction can be written as

$$\left.\begin{array}{l} A = A_0 \mathrm{sech}^2 \sqrt{\dfrac{A_0}{2}}(\zeta + Y\tan\psi - Cs), \\[2mm] C = \dfrac{1}{2}A_0 + \dfrac{3}{4}\tan^2\psi, \end{array}\right\} \tag{10}$$

where A_0 is the wave amplitude, C is the phase speed, and the crest line has a slope $\tan\psi$, measured counterclockwise from the Y-axis, see Figure 1. Then, the V-shaped wave composed of two internal solitary waves can be obtained by adding two waves as described in Equation 10; thereby, referring to the transformation (Equation 9), the initial waves inserted in Equation 5 for numerical results can be constructed as

$$\left\{\begin{array}{l} \xi(X, y, \tau = 0) = \xi_1^0(X, y) + \xi_2^0(X, y), \\[2mm] \xi_1^0 = \xi_1 H(y)\mathrm{sech}^2 \sqrt{\dfrac{\xi_1}{2}}(X - y\tan\psi_0), \\[2mm] \xi_2^0 = \xi_2 H(-y)\mathrm{sech}^2 \sqrt{\dfrac{\xi_2}{2}}(X + y\tan\psi_0), \end{array}\right. \tag{11}$$

where ξ_1 and ξ_2 are the amplitudes of the upper ($y > 0$) and lower ($y < 0$) branches, respectively, and ψ_0 is the inclination angle. $H(y)$ is the Heaviside step function, which equals 0 for $y < 0$ and 1 for $y \geq 0$. A sketch of the initial wave is illustrated in Figure 1a, together with three potential subsequent evolution scenarios. A large number of remote sensing images confirm the frequent occurrence of these three types of ISW wave-wave interaction in the ocean and some examples are also exhibited in Figure 1.
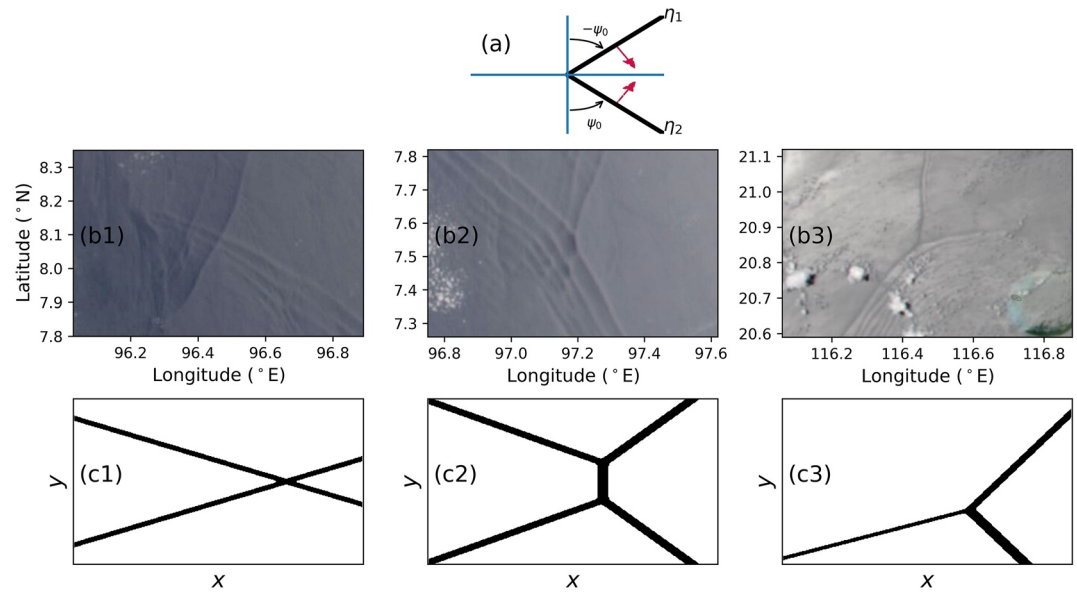
Figure 1. A sketch of the initial V-shaped wave with respective amplitudes (η_1, η_2), inclination angles ($-\psi_0$, ψ_0) and propagation directions (purple arrows) is shown in panel (a). Three types of frequently observed internal solitary wave-wave interactions are illustrated in panels (b1–b3), whose theoretical delineations evolving from the initial V-shaped wave are also shown in panels (c1–c3), indicating a significant similarity. These three scenarios are, respectively, labeled as Experiment 1, Experiment 2 and Experiment 3 hereafter. The satellite remote sensing images are obtained from the NASA Worldview (https://worldview.earthdata.nasa.gov), and panels (b1–b2) were photographed on 21 August 2020, whereas (b3) was on 24 May 2021.

Note that Yuan, Grimshaw, Johnson, and Wang (2018) categorized the evolution of the initial V-shaped wave into six types, in addition to singular points, on the basis of analytical solutions to the KP equation. Among them, two pairs of evolution scenarios can be transformed via an inversion of symmetry; they possess the same dynamical features. Thus, there are four distinguished evolution scenarios for the initial V-shaped wave; however, one of them (case (e) or (f) of Figure 2 in Yuan, Grimshaw, Johnson, and Wang (2018)) has very complex structures and is susceptible to environmental background factors, which implies it is presumably more difficult to be recorded in the ocean. In this paper, we consider the three frequently observed evolution patterns, as shown in Figure 1.

2.3. Boundary Conditions and Numerical Methods

To thoroughly investigate the evolution of the initial V-shaped wave, here we implement a window-scheme method (Schlatter et al., 2005) to suppress the dispersion effects induced by the open boundary, which confines our attention to the small interaction zone where the edges of wave crest lines have negligible impact. Essentially, it is a decomposition of ξ in Equation 5,

$$\xi = W\xi + (1 - W)\xi = \zeta + (1 - W)\xi, \tag{12}$$

where $W(y)$ is a window function, defined as

$$W(y) = \exp\left(-a\left|\frac{y}{L_y}\right|^n\right), \tag{13}$$

with $n = 95$ and $a = 1.02^n \ln 10$ after some pre-tests. Now ζ represents the interior component, which equals unity in a specified region $|y| \ll L_y$ and rapidly tapers to zero in the artificial boundary layers $|y| > L_y$. It remains to resolve the component in the artificial boundary layers and note that the analytical solution ξ is known when the environmental background is uniform, that is no rotation and varying topography are included. Thus it is supposed that in the artificial boundary layers $|y| > L_y$, the analytical solution ξ^0 in the form (Equation 11), but moving with the corresponding phase speed, is used. Nonetheless, here the rotation and shoaling topography are considered, and the adapted ξ^0 is not a solution, thus the inconsistency rendered at $y = \pm L_y$ would contaminate the

inner domain for long-time evolution. This error is generally small and propagates with the finite wave speed. So in the following numerical computations, the spatial range along the transverse y direction is chosen large enough to ensure that the central interaction region is not perceptibly affected by this error during the calculation time.

Now we illustrate the ultimate expression of the vKP equation incorporating the window-scheme method in numerics. We substitute

$$\xi = \zeta + (1 - W)\xi^0 \tag{14}$$

into Equation 5, and it follows that

$$[\zeta_\tau + \mu\zeta\zeta_X + \zeta_{XXX}]_X + \sigma\zeta_{yy} - \kappa\zeta = G_1(X, y, \tau) + G_2(X, y, \tau), \tag{15}$$

where

$$G_1(X, y, \tau) = -(1 - W)\left[\left(\xi^0_\tau + \mu\xi^0\xi^0_X + \xi^0_{XXX}\right)_X + \sigma\xi^0_{yy} - \kappa\xi^0\right],$$

$$G_2(X, y, \tau) = \mu(1 - W)\left[W\xi^0\xi^0_X - \left(\zeta\xi^0\right)_X\right]_X + \sigma\left(2W_y\xi^0_y + W_{yy}\xi^0\right).$$

Since we have assumed that ξ^0 satisfies the vKP Equation 5 in the boundary layers, $G_1 \equiv 0$. Considering here the coefficients μ, σ, and κ defined in Equation 6 vary with τ, Equation 15 is numerically solved using a hybrid discretization scheme in space with the pseudo-spectra method in the X direction and the fourth-order central finite difference method in the y direction. We rewrite Equation 15 as

$$\left[\zeta_\tau + \frac{1}{2}\mu\left(\zeta^2\right)_X + \zeta_{XXX}\right]_X + \sigma\zeta_{yy} - \kappa\zeta = G_2. \tag{16}$$

Then taking the Fourier Transform in the X direction yields

$$ik\left(\hat{\zeta}_\tau + \frac{1}{2}ik\mu\widehat{\zeta^2} - ik^3\hat{\zeta}\right) + \sigma\widehat{\zeta_{yy}} - \kappa\hat{\zeta} = \widehat{G_2}, \tag{17}$$

where $\hat{\cdot}$ indicates the Fourier Transform and k is the wavenumber in Fourier space. To circumvent the stiffness problem and use large time step to increase the computational efficiency, we multiply the above equation by the integrating factor $e^{-ik^3\tau}$. After a straightforward calculation, Equation 17 becomes

$$ik\left(\widehat{M}_\tau + \frac{1}{2}ike^{-ik^3\tau}\mu\widehat{\zeta^2}\right) + \sigma e^{-ik^3\tau}\widehat{\zeta_{yy}} - \kappa\widehat{M} = e^{-ik^3\tau}\widehat{G_2}, \tag{18}$$

where $\widehat{M} = e^{-ik^3\tau}\hat{\zeta}$. Next, we express ξ in forms of M; thus, the equation can be rewritten as

$$ik\left\{\widehat{M}_\tau + \frac{1}{2}ike^{-ik^3\tau}\mu\mathcal{F}\left[\left(\mathcal{F}^{-1}\left(e^{ik^3\tau}\widehat{M}\right)\right)^2\right]\right\} +$$
$$\sigma e^{-ik^3\tau}\left\{\mathcal{F}\left[\left(\mathcal{F}^{-1}\left(e^{ik^3\tau}\widehat{M}\right)\right)_{yy}\right]\right\} - \kappa\widehat{M} = e^{-ik^3\tau}\widehat{G_2}, \tag{19}$$

where $\mathcal{F}$ is the Fourier Transform operator. The term ∂_y^2 is approximated by the fourth-order central finite difference method. To ensure numerical accuracy, 2,048 modes and 2,000 grid points are selected along the respective propagation X and transverse y direction. In the time domain, the fourth-order Runge-Kutta iteration scheme is invoked with step 1.0 in the transformed variables τ. Finally, to illuminate the results in physical space, the value of ζ is transformed back to η through Equation 4.

3. Wave-Wave Interactions

We investigate three frequently observed ISW wave-wave interactions as shown in Figure 1, which are hereafter referred to as Experiment 1 (panel (c1)), Experiment 2 (panel (c2)), and Experiment 3 (panel (c3)), respectively. The specific set-ups of experiments are illustrated in Table 1. The computational domain is $x \times y = [0, 300] \times [-400, 400]$ km^2, and an idealized y-independent shoaling topography $h(x)$ ranging from 500 to 200 m lies along the x-axis, see Figure 2. The density profile is calculated through the Equation of State using the monthly averaged temperature and salinity data at 117.5°E, 21°N in the South China Sea, taken from the World Ocean

Table 1
The Set-Ups of Experiments

Experiment labels	Amplitude of upper branch η_1 (m)	Amplitude of lower branch η_2 (m)	Inclination angle ψ_0 (°)	Rotation f (s^{-1})
1 (1)	−15	−15	16	0
1 (2)	−15	−15	16	2.5×10^{-5}
1 (3)	−15	−15	16	5×10^{-5}
1 (4)	−15	−15	16	7.5×10^{-5}
1 (5)	−15	−15	16	1×10^{-4}
2 (1)	−20	−20	8	0
2 (2)	−20	−20	8	2.5×10^{-5}
2 (3)	−20	−20	8	5×10^{-5}
2 (4)	−20	−20	8	7.5×10^{-5}
2 (5)	−20	−20	8	1×10^{-4}
3 (1)	−25	−10	3.67	0
3 (2)	−25	−10	3.67	2.5×10^{-5}
3 (3)	−25	−10	3.67	5×10^{-5}
3 (4)	−25	−10	3.67	7.5×10^{-5}
3 (5)	−25	−10	3.67	1×10^{-4}

Atlas (WOA) 2013. Facilitated by the obtained density distribution, the buoyancy frequency N, the modal function ϕ, and linear wave phase speed c in Equation 2 are numerically solved, see Figure 2.

To comprehensively understand the dynamical role of shoaling topography and the Earth's rotation on ISW wave-wave interactions, the following numerical results consider the cases with/without varying topography and involve the Earth's rotation of different strength, $f = 0, 2.5 \times 10^{-5}, 5.0 \times 10^{-5}, 7.5 \times 10^{-5}, 1.0 \times 10^{-4}$ s^{-1}, corresponding to latitudes $\varphi = 0°, 9.9°, 20.1°, 30.9°, 43.3°$N, where internal solitary waves have been frequently recorded (Jackson, 2004).

3.1. Experiment 1: Rotational Effect

We examine Experiment 1 with constant topography. Here the initial V-shaped wave has respective amplitudes $\eta_1 = \eta_2 = -15$ m for the two branches and inclination angle $\psi_0 = 16°$ (here the minus signs of amplitudes signify depression waves and do not affect the magnitude comparison), whose evolution regime falls into the scenarios akin to panel (b1) in Figure 1. When the rotational effect is absent, in a constant depth of $h = 500$ m, the initial V-shaped wave evolves to the so-called X-shaped wave featuring a phase shift in the interaction zone whose maximal amplitude could be four times that of the initial wave (double the superposition of the initial two branches) and a curved trailing wave train with positive polarity (also known
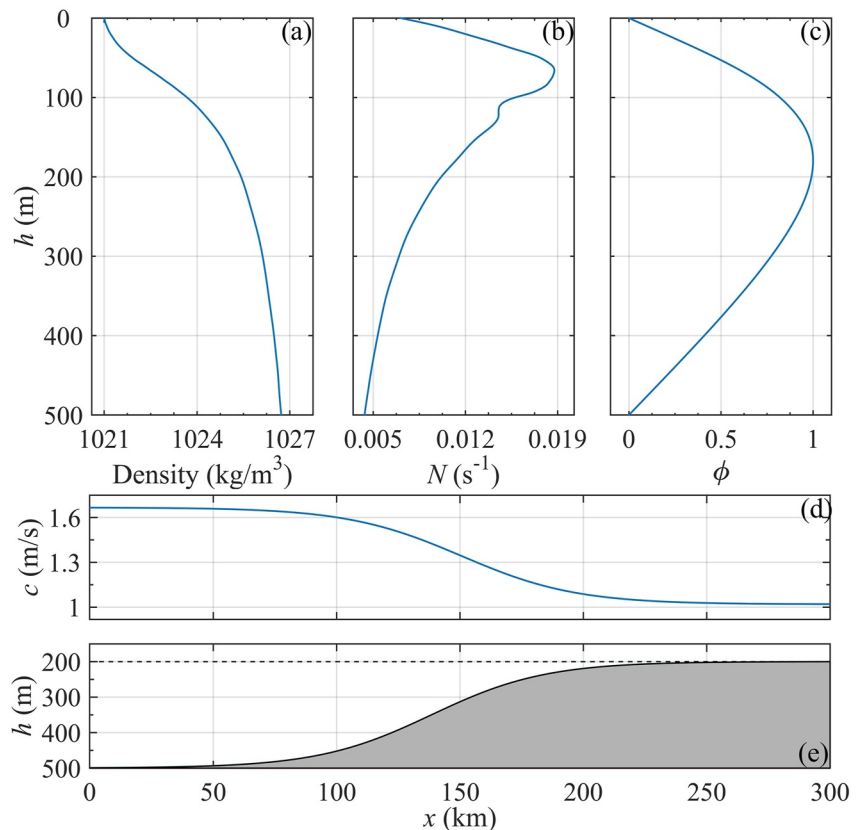

Figure 2. Panel (a) is the density profile ρ_0 used in the calculations, which is obtained at 117.5°E, 21°N in the South China Sea from the WOA data set, (b) the buoyancy frequency N, (c) the modal function ϕ in equation 2, (d) the linear phase speed c of long mode-1 ISWs in the absence of rotational effects, and (e) the y-independent depth $h(x)$.
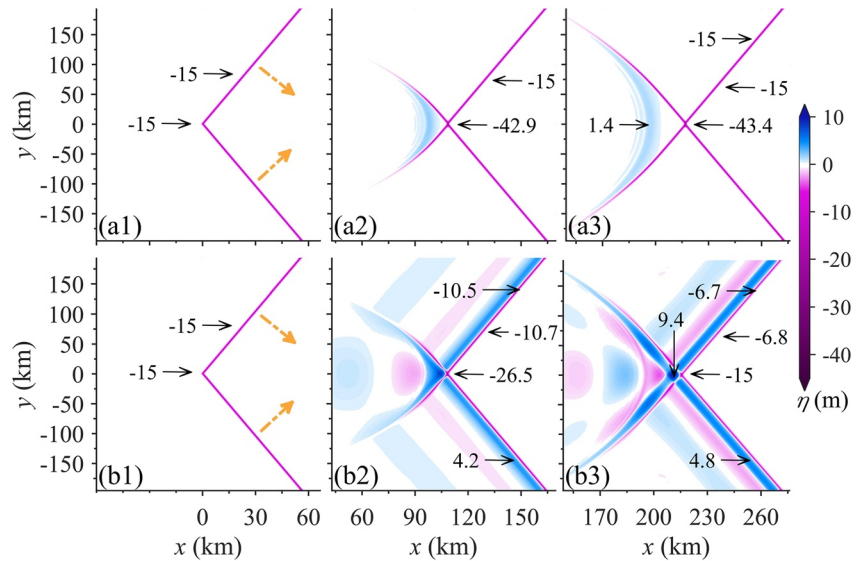
Figure 3. Experiment 1 with a uniform depth of 500 m and inclination angle $\psi_0 = 16°$. Panels (a1–a3) are selected to exhibit the evolution of wave amplitudes when the rotation and shoaling topography are absent at time $t = 0$, 16.6, and 33.2 hr, respectively. In contrast, panels (b1–b3) are for the cases with rotation parameter $f = 1.0 \times 10^{-4}$ s^{-1} (flat bottom), at the same frame as in the top row. To exhibit the wave patterns in detail, the amplitudes η in regions specified by black arrows and the propagation directions of initial waves indicated by yellow dashed arrows are emphasized, respectively.

as an elevation wave) occurs at the rear of leading waves due to conservation of mass, see panels (a1–a3) in Figure 3 and Yuan, Grimshaw, Johnson, and Wang (2018) for more details.

The attempt to take the Earth's rotation ($f = 1.0 \times 10^{-4}$ s^{-1} at first) into consideration results in a train of oscillatory waves due to the additional long-wave dispersion exerted by the rotation, destroying the essential balance between the nonlinearity and dispersion of ISWs, which features wave patterns akin to the negative leading X-shaped waves, but with the positive polarity, and some other small waves occur at the rear, see panels (b2–b3) in Figure 3. More importantly, these two X-waves possessing opposite polarities intersect near the interaction zone. This superimposition renders two symmetric regions with zero wave amplitudes, which manifests as two blank patches approximately at $y = \pm 10$ km, cutting off the two otherwise coherent X-shaped waves as shown in Figure 4b1.

As expected, rotation diminishes the wave amplitudes. It is shown in Figures 3 and 4 that the leading wave amplitude at the interaction midpoint is -15 m at time $t = 33.2$ hr, much smaller than its counterpart of -43.4 m when no rotation is considered. When rotation is not included the midpoint amplitude undergoes a rapid increase at first after which the growth rate decreases as the amplitude asymptotically approaches the theoretical maximum value -45 m as revealed by the blue X-marked lines ($f = 0$) in Figure 5a, see the theoretical predictions in Yuan, Grimshaw, Johnson, and Wang (2018). However, when rotation is considered, the results are different. Since rotation needs a relatively long-time accumulation to have a conspicuous impact, initially the nonlinearity induced by wave resonance overwhelmingly dominants the evolution, and the midpoint amplitude keeps increasing, but afterward, when rotational effects become important and come into play, it manifests itself by decreasing the amplitude almost linearly with time, see the results when $f \neq 0$ in Figure 5a. To gain more insights on rotational effects, we examine the ratios η_a/η_b of wave amplitudes in the interaction zone (η_a) in Figure 5c to amplitudes of upper branch waves far away from the interaction zone (η_b). One of most remarkable features is that stronger rotations render more severe reductions of the amplitudes in the interaction zone compared with the regions far away from the interaction zone.

Due to conservation of mass, the decrease of the leading X-shaped wave nourishes the sprout of a secondary X-shaped wave and small radiating wave trains (Figure 4). A noticeable feature is the intersection point of the secondary positive X-shaped wave, whose amplitude increases with time. When rotation is absent, the amplitude of the leading one is slightly larger than the rear one for the ultimate X-shaped wave, as the reverse polarity trailing waves occur at the cost of rear waves, see Figure 4a2. Nonetheless, the rotation modulates this character, and the trend could be reversal; see panels (b1) and (b2).
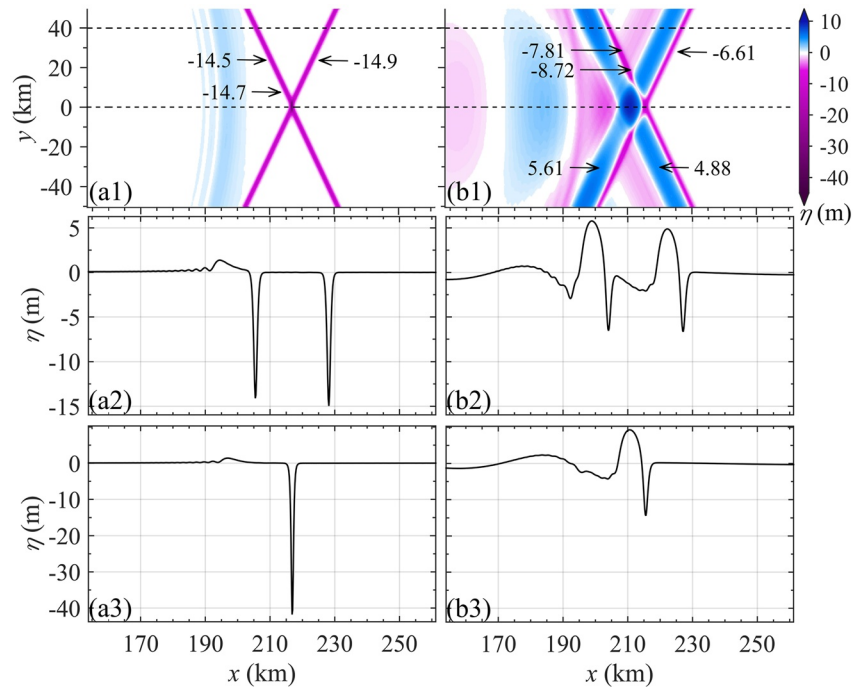
Figure 4. Panels (a1) and (b1) are the respective zoom-ins of panels (a3) and (b3) in Figure 3, where the amplitudes η in regions specified by black arrows are emphasized. Their corresponding wave amplitudes along $y = 40$ km and $y = 0$ are shown in panels (a2–a3) and (b2–b3), respectively. The time is at $t = 33.2$ hr.

The strength of rotation plays a vital role in modulating wave-wave interactions. We supplement the cases with Coriolis parameters $f = 2.5 \times 10^{-5}, 5.0 \times 10^{-5}, 7.5 \times 10^{-5}$ s^{-1}, as shown in Figure 6. The magnitude of rotation impacts the diminution of the leading X-shaped wave, the emergence of the secondary X-shaped wave, and the interference between them. From the perspective of long-time evolution, larger rotational terms reduce the increase of leading wave amplitude induced by wave resonance more quickly and commence the decrease earlier (Figure 5a).To quantify this point, the Ostrovsky number O_s measuring the competition of the nonlinear and rotational terms (Farmer et al., 2009) is defined by

$$O_s = -\frac{24\pi^2 c\alpha\eta}{f^2 L^2},\tag{20}$$

where L is the typical horizontal scale. For $O_s \ll 1$, rotation becomes significant. Here the O_s is 0.074, 0.13, 0.30, and 1.2, respectively, in the order of largest to smallest f, as in Figure 6, which justifies the statement mentioned above.

3.2. Experiment 1: Combined Effect of Rotation and Topography

When shoaling topography is considered, the evolution scenarios become significantly disparate from those with a flat bottom (panels a1–a3 of Figure 3 vs. those of Figure 7). No perceptible diversities can be remarked on prior to the initial V-shaped wave approaching the continental slope. Nevertheless, as the waves at two edges start to climb up the topography, their amplitudes are amplified, whereas their propagation speeds are slackened. Over time this tendency spreads to the wave-wave interaction zone, which amounts to decreasing the magnitude of inclination angle ψ_0 (Figure 1). Then, a Mach stem, whose length along the y direction increases with time and whose amplitude along the y direction almost keeps uniform (Figure 8a1), develops from the interaction zone, different from the midpoint of the X-shaped wave for the absence of varying topography, see Figure 7a3 or Figure 8a1. The emergence of the Mach stem presumably implies the importance of shoaling topography on ISW wave-wave interactions. It is also indicative of high nonlinearity and a complicated wave resonance. In addition, small trailing waves with the same polarity as the leading waves emerge, followed by the trailing wave train with the opposite polarity, akin to the scenarios for the flat bottom.
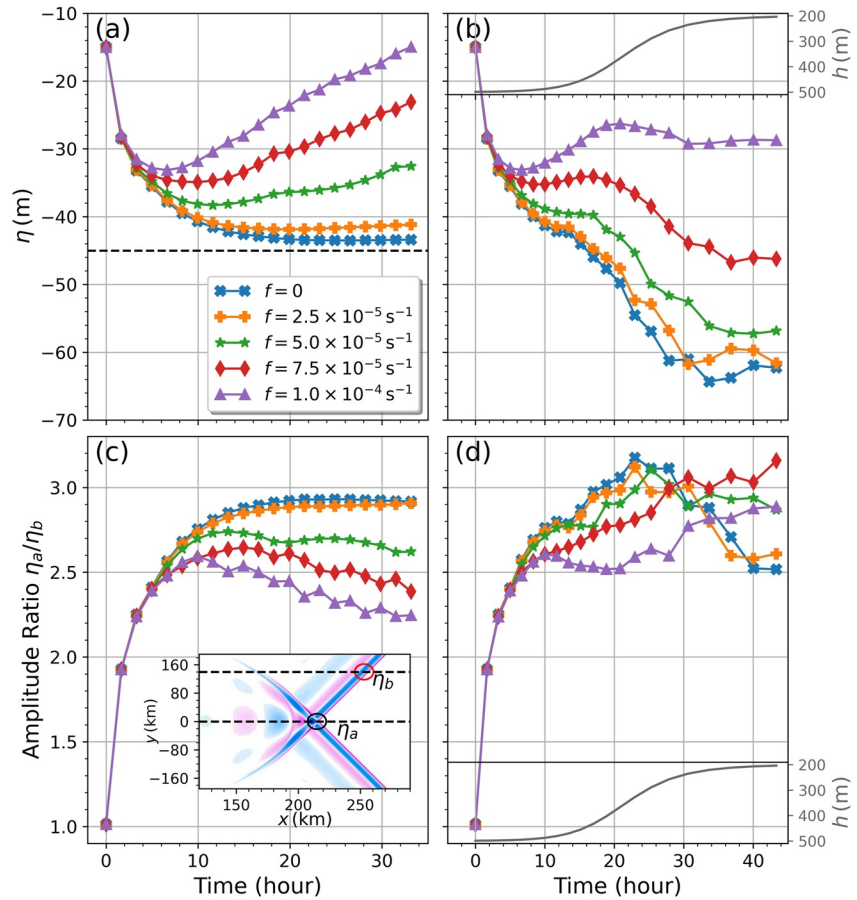
Figure 5. The time series of amplitudes in the middle of interaction zone (indicated by the black circle in the insets of panel (c)) are shown in panel (a) for the scenarios of flat bottom and their ratios to amplitudes of upper branch waves along $y = 140$ km (indicated by the red circle in the insets of panel (c)) are shown in panel (c), while the panels (b) and (d) are for the scenarios of shoaling topography. Note that the results with different rotational parameters are exhibited with different colored marked lines and the dark dashed line in panel (a) implies the theoretical maximum value -45 m. The insets in panels (b) and (d) indicate the water depth at specific times.

Suppose the rotation with $f = 1.0 \times 10^{-4}$ s^{-1} is taken into account together with the shoaling topography. In that case, the most discernible characteristic should be the suppression of the Mach stem, resulting in an interaction pattern plausibly similar to its counterpart without shoaling topography, albeit the amplitudes and waveforms are different in a subtle way, see Figures 3b3 and 7b3 or more clearly, Figures 4b1 and 8b1. It is clear that the presence of rotation hinders the wave resonance and the development of the Mach stem. Moreover, to understand its long-time evolution, we elongate the computation time to 60 hr with a larger domain; however, the Mach stem still fails to occur (figures not shown).

It is worthwhile to illustrate the combined effect of rotation ($f = 1.0 \times 10^{-4}$ s^{-1}) and shoaling topography on ISW wave-wave interactions. At time $t < 6$ hr, the accumulation of rotational effect is insufficient to generate perceptible changes and the waves still propagate over the nearly flat continental shelf, whereby the dynamics are almost the same as those without rotation and varying topography, embodying the character of a drastic increase of midpoint wave amplitudes at the interaction zone, see purple triangular solid lines in Figure 5b. Then at $6 < t < 18$ hr, rotation starts to exert appreciable influence on the wave evolution, manifesting as the decrease of midpoint wave amplitude. Afterward, the waves climb up the continental slope, and the effect of shoaling topography comes into play in the evolution, which leads to additional nonlinearity and competes with the dispersion induced by the rotation, resulting in a delicate magnification of amplitudes until the waves thoroughly propagate into the shallow water at time $t = 30$ hr. After that, the midpoint amplitude tends to be constant, although the effects of rotation seems to be slightly stronger than the shoaling topography. Moreover, a comparison between panels (a) and (b) in Figure 5 conspicuously illuminates the augmentation of amplitudes by the shoaling topography. The
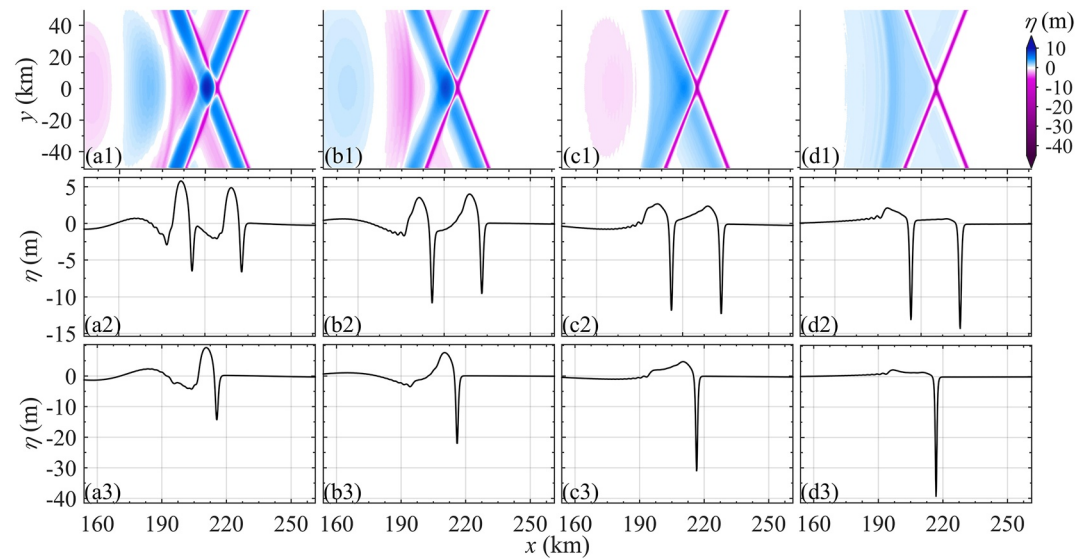
Figure 6. The top row is the horizontal view of amplitudes for Experiment 1 under $f = 1.0 \times 10^{-4}$, 7.5×10^{-5}, 5.0×10^{-5}, 2.5×10^{-5} s^{-1} (flat bottom) in panels (a1–d1), respectively. The corresponding amplitudes along $y = 40$ km and $y = 0$ are exhibited in the second row (a2–d2) and the third row (a3–d3), respectively. The topography here is uniform, and the time is at $t = 33.2$ hr.

amplitude ratios η_a/η_b shown in Figure 5d show that the combined effects of shoaling topography and rotation impose more influence on wave amplitudes in the interaction zone than in regions far away from the interaction zone and surprisingly, the largest ratios emerge at medium rotation, here $f = 7.5 \times 10^{-5}$ s^{-1}, presumably due to the complicated wave resonance occurs at the interaction zone.

Accompanied by the aforementioned variation of midpoint amplitude, the trailing waves develop and exhibit complicated patterns whose complexity is closely related to the magnitude of rotation, as shown in Figure 9. It is clear that the wave dynamics manifest the nonlinear interference of the rotation, shoaling topography, and the essential resonance of ISW wave-wave interactions. When rotation becomes significant, the emergence of the Mach stem is inhibited.
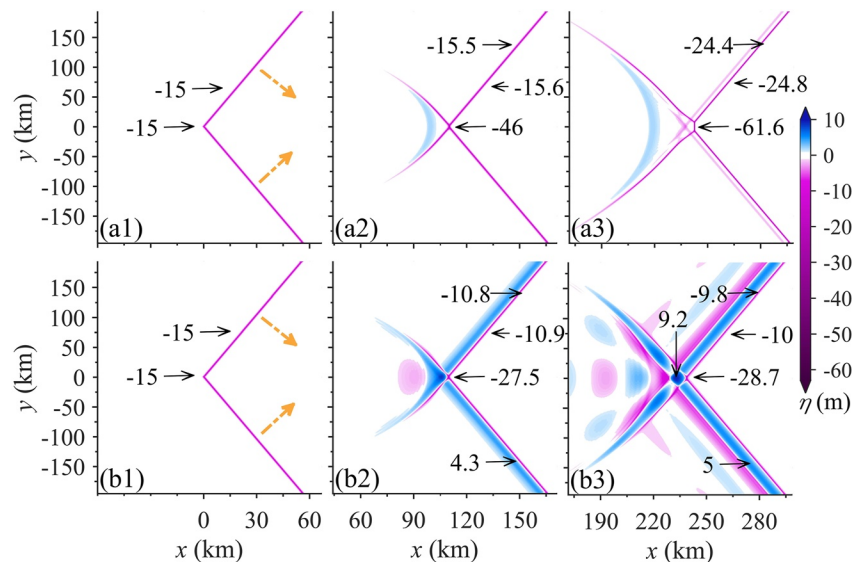

Figure 7. Experiment 1 with shoaling topography. Panels (a1–a3) are selected to exhibit the evolution of wave amplitudes when the rotation is absent at time $t = 0$, 17.0, and 43.3 hr, respectively. In contrast, panels (b1–b3) are for the cases with rotation parameter $f = 1.0 \times 10^{-4}$ s^{-1} (note that shoaling topography is in presence), and the layout is same as the top row. To exhibit the wave patterns in detail, the amplitudes η in regions specified by black arrows and the propagation directions of initial waves indicated by yellow dashed arrows are emphasized, respectively.
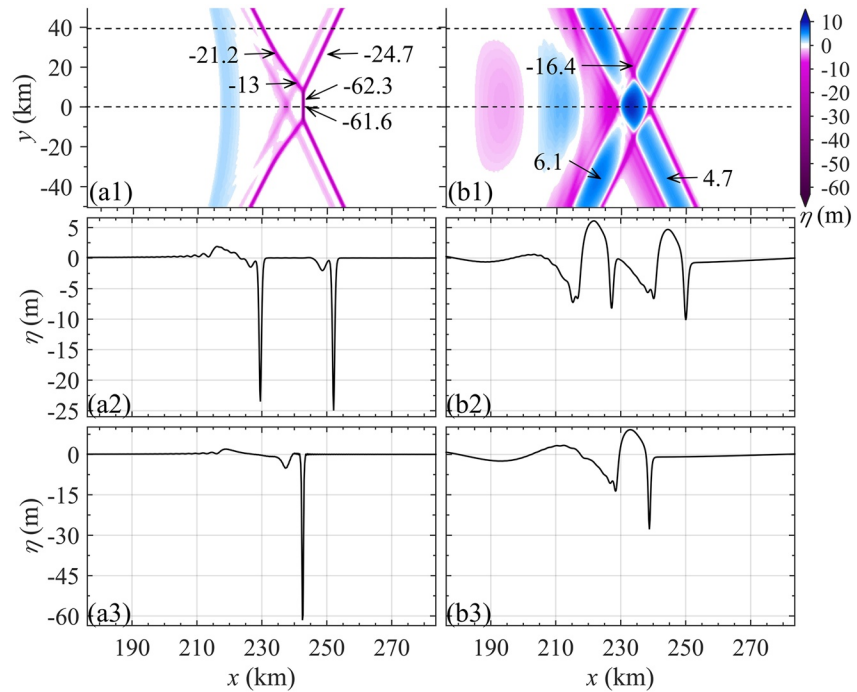
Figure 8. Panels (a1) and (b1) are the respective zoom-ins of panels (a3) and (b3) in Figure 7, where the amplitudes η in regions specified by black arrows are emphasized. Their corresponding wave amplitudes η along $y = 40$ km and $y = 0$ are shown in panels (a2–a3) and (b2–b3), respectively. The time is at $t = 43.3$ hr.

3.3. Experiment 2: Rotational Effect

In Experiment 1, one of the results induced by the combined effect of the rotation and topography on ISW wave-wave interactions is the generation and evolution of the Mach stem; thus, in this section, we further investigate this issue. Here the initial waves have the respective amplitudes $\eta_1 = \eta_2 = -20$ m and the inclination angle has been selected to $\psi_0 = 8°$ (hereafter labeled as Experiment 2), whose evolution regime falls into the
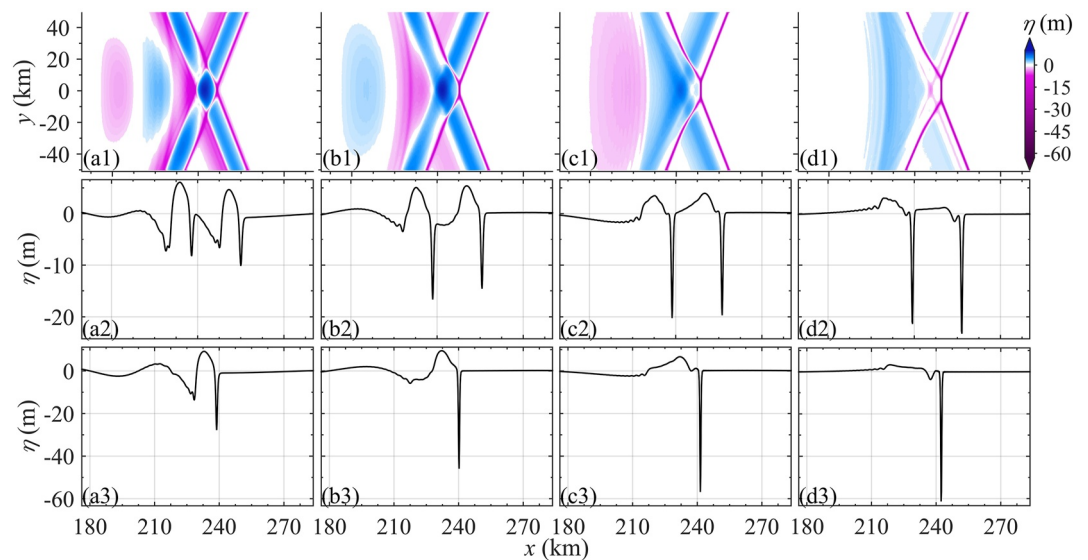

Figure 9. The top row is the horizontal view of wave amplitude for Experiment 1 under the circumstance of shoaling topography and rotation parameters $f = 1.0 \times 10^{-4}$, 7.5×10^{-5}, 5.0×10^{-5}, 2.5×10^{-5} s^{-1} in panels (a1–d1), respectively. The corresponding amplitudes along $y = 40$ km and $y = 0$ are exhibited in the second row (a2–d2) and the third row (a3–d3), respectively. The shoaling topography is shown in Figure 2, and the time is at $t = 43.3$ hr.
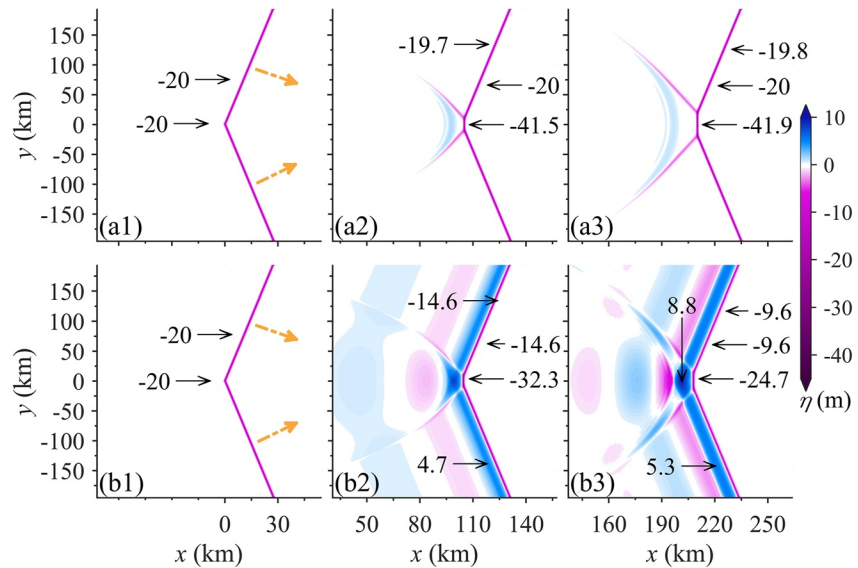
Figure 10. Experiment 2 with uniform depth 500 m and inclination angle $\psi_0 = 8°$. Panels (a1–a3) are selected to exhibit the evolution of wave amplitudes when rotation and shoaling topography are absent at time $t = 0$, 16.6, and 33.2 hr, respectively. In contrast, panels (b1-b3) are for the cases with rotation parameter $f = 1.0 \times 10^{-4}$ s^{-1} (flat bottom), and the layout is same as the top row. To exhibit the wave patterns in detail, the amplitudes η in regions specified by black arrows and the propagation directions of initial waves indicated by yellow dashed arrows are emphasized, respectively.

scenarios akin to panel (c2) in Figure 1. When rotation is absent, and the ISW wave-wave interactions occur over a flat bottom, a Mach stem arises in the interaction zone, and its length along the y direction increases linearly with time while its amplitude is approximately twice the initial wave, see panels (a1–a3) in Figure 10. In addition, two post-interaction wave branches (with an amplitude of -4 m) are much smaller than the two initial wave branches (with an amplitude of -20 m) and the Mach stem (with an amplitude of -42 m), as shown in Figures 11a1–11a3.

When rotation ($f = 1.0 \times 10^{-4}$ s^{-1}) is considered, the emergence of trailing waves with opposite polarity in the rear of leading waves is similar to that of Experiment 1. Nevertheless, distinguished from the ultimate extinction in Experiment 1, here the Mach stem is more robust and can resist the strong rotation ($f = 1.0 \times 10^{-4}$ s^{-1} amounts to those at a latitude of 43.3°N), although the length and strength are mitigated; see the comparisons between panels (a1–a3) and (b1–b3) in Figure 11. More importantly, the incorporation of rotation considerably perturbs wave-wave interactions, whereby the two post-interaction wave branches (inside the red rectangular boxes of Figure 11) are disintegrated and difficult to identify from the intricate trailing waves, even for relatively weak rotational effect $f = 5.0 \times 10^{-5}$ s^{-1} (at low latitude 20.1°N); see Figure 12. This property plausibly explains the indistinctness of the two wave branches when a Mach stem is clearly recorded in satellite images; see Figure 1a2 for instance. Indeed, by MITgcm numerical simulation results, Shimizu and Nakayama (2017) identified the Mach stem originating from oblique ISW wave-wave interactions at ~9°N ($f = 2.3 \times 10^{-5}$ s^{-1}). In their Figures 4 and 9, one of the post-interaction branches is almost invisible, which is very similar to our experiments. It is clear that stronger rotation renders smaller leading wave amplitudes, more complicated trailing wave patterns, and a shorter and weaker Mach stem (Figure 12). Moreover, the effect of rotation in this experiment is supposed to be weaker than that in Experiment 1, as the Ostrovsky number O_s (Equation 20) is proportional to wave amplitudes which are larger in this experiment, recalling that $O_s \ll 1$ signifies a significant rotational effect.

3.4. Experiment 2: Combined Effect of Rotation and Topography

Now we investigate the individual effect of shoaling topography as shown in Figure 13. In addition to the generation of two categories of trailing waves, one with the same polarity and the other with opposite polarity as the leading waves, the most remarkable feature is that the Mach stem is slightly arched with a smaller amplitude at the midpoint, however, propagating faster than its periphery, see the specific magnitude in Figure 14a1,
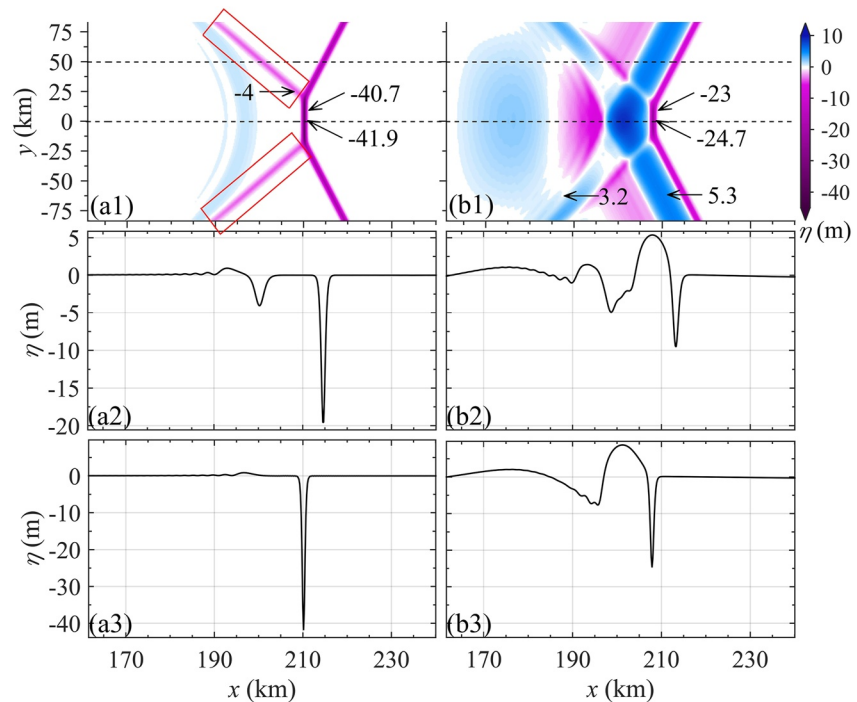
Figure 11. Panels (a1) and (b1) are the respective zoom-ins of panels (a3) and (b3) in Figure 10, where the amplitudes η in regions specified by black arrows are emphasized. Their corresponding wave amplitudes along $y = 40$ km and $y = 0$ are shown in panels (a2–a3) and (b2–b3), respectively. Note that the red rectangular boxes in (a1) accentuate the post-interaction waves, and the time is at $t = 33.2$ hr.

seemingly contradicting the wave theory. Nevertheless, this naturally occurring paradox presumably designates the complexity of nonlinearity.

Finally, we examine the combined effect of rotation and shoaling topography on ISW wave-wave interactions. It is clear that the scenarios are different from the cases considering individual rotational or topographic effects. These two factors jointly lead to nascent trailing wave packets at $x = 220$ km in Figure 14b3). After sufficiently
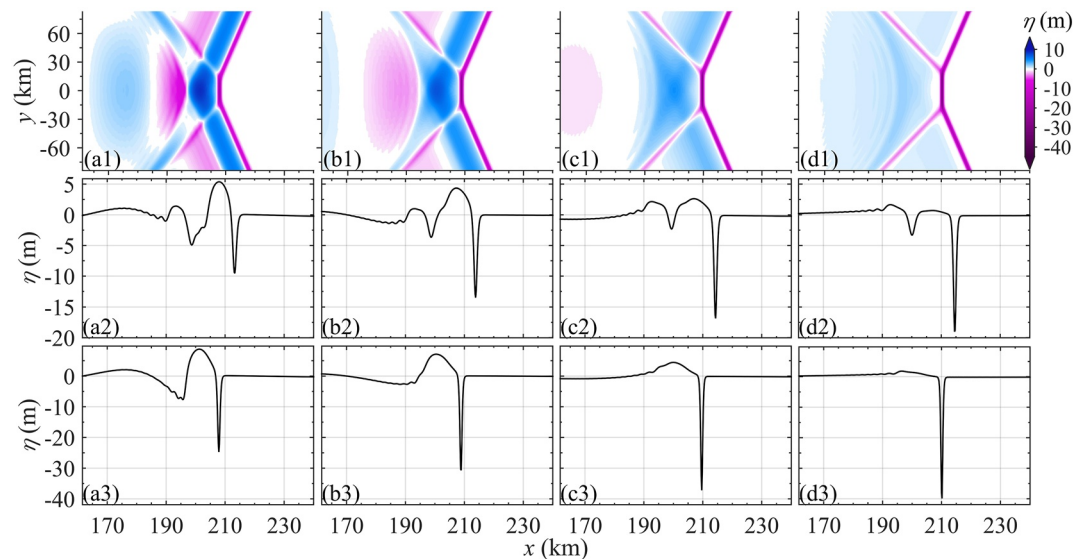

Figure 12. The top row is the horizontal view of wave amplitude for Experiment 2 under the circumstance of $f = 1.0 \times 10^{-4}$, 7.5×10^{-5}, 5.0×10^{-5}, 2.5×10^{-5} s^{-1} (flat bottom) in panels (a1–d1), respectively. The corresponding amplitudes along $y = 40$ km and $y = 0$ are exhibited in the second row (a2–d2) and the third row (a3–d3), respectively. The time is at $t = 33.2$ hr.
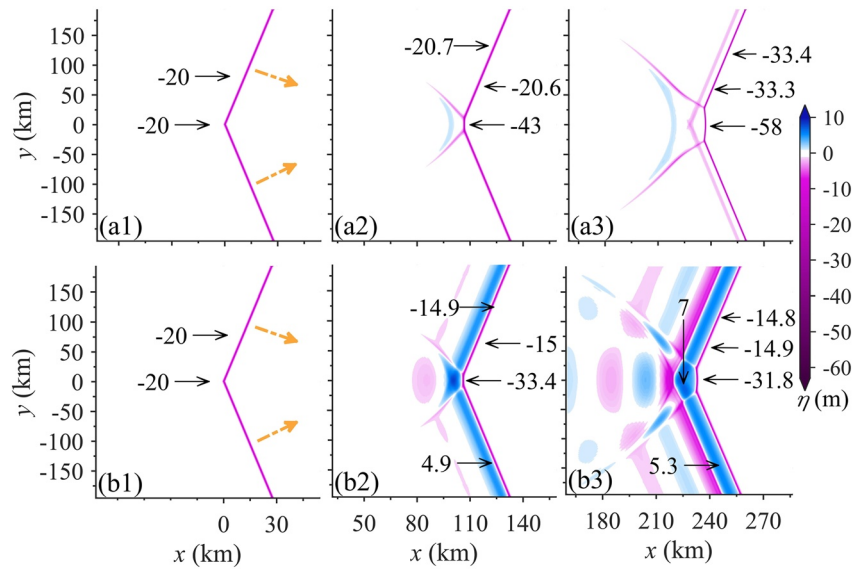
Figure 13. Experiment 2 with shoaling topography as shown in Figure 2. Panels (a1–a3) are selected to exhibit the evolution of wave amplitudes in the absence of rotation at time $t = 0$, 17.0, and 43.3 hr, respectively. In contrast, panels (b1–b3) are for the cases with rotation parameter $f = 1.0 \times 10^{-4}$ s^{-1} (note that shoaling topography is in presence), and the layout is same as the top row. To exhibit the wave patterns in detail, the amplitudes η in regions specified by black arrows and the propagation directions of initial waves indicated by yellow dashed arrows are emphasized, respectively.

long time, it develops into a KdV-like undular bore, as found in Grimshaw et al. (2014). Nevertheless, the absence of this striking feature for the cases with smaller f (Figure 15) indicates that this is a subtle result in which rotation perturbs the trailing waves to a point where the nonlinear effect induced by topography comes into play and steepens the waves to generate such steep wave packets.
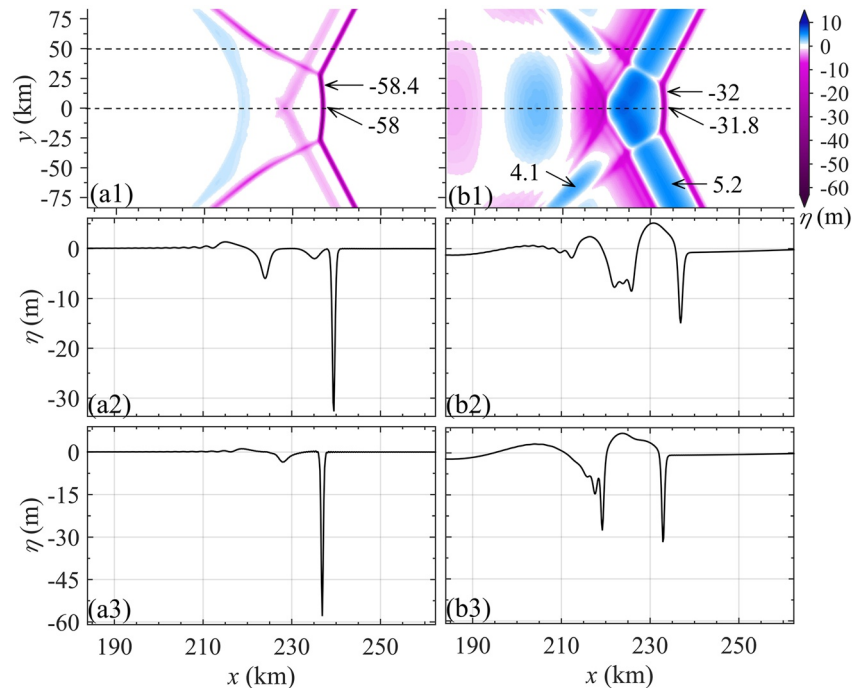

Figure 14. Panels (a1) and (b1) are the respective zoom-ins of panels (a3) and (b3) in Figure 13, where the amplitudes η in regions specified by black arrows are emphasized. Their corresponding wave amplitudes along $y = 40$ km and $y = 0$ are shown in panels (a2–a3) and (b2–b3), respectively. The time is at $t = 43.3$ hr.
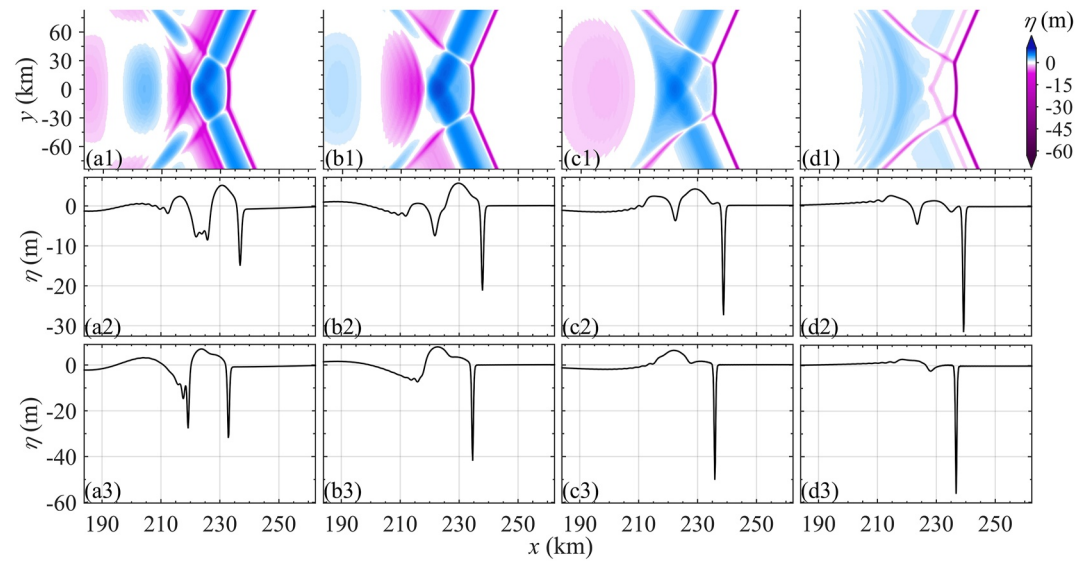
Figure 15. The top row is the horizontal view of wave amplitude for Experiment 2 under the circumstance of shoaling topography and rotation parameters $f = 1.0 \times 10^{-4}$, 7.5×10^{-5}, 5.0×10^{-5}, 2.5×10^{-5} s^{-1} in panels (a1–d1), respectively. The corresponding amplitudes along $y = 40$ km and $y = 0$ are exhibited in the second row (a2–d2) and the third row (a3–d3), respectively. The shoaling topography is shown in Figure 2, and the time is at $t = 43.3$ hr.

3.5. Experiment 3: Rotational Effect

In this section, we examine wave-wave interaction scenarios as shown in panel (c3) of Figure 1. Thus the initial amplitudes are chosen to be $\eta_1 = -25$ m and $\eta_2 = -10$ m, respectively, and the inclination angle $\psi_0 = 3.67°$. These cases, hereafter, are labeled as Experiment 3. The oblique ISW wave-wave interactions that occur over flat bottom without rotation are shown in Figure 16. Note that the remarkable characteristic is the appearance of a third wave branch originating from the interaction point whose amplitude is closely related to the amplitudes of the initial two wave branches; the interested readers are referred to Yuan, Grimshaw, Johnson, and Wang (2018)
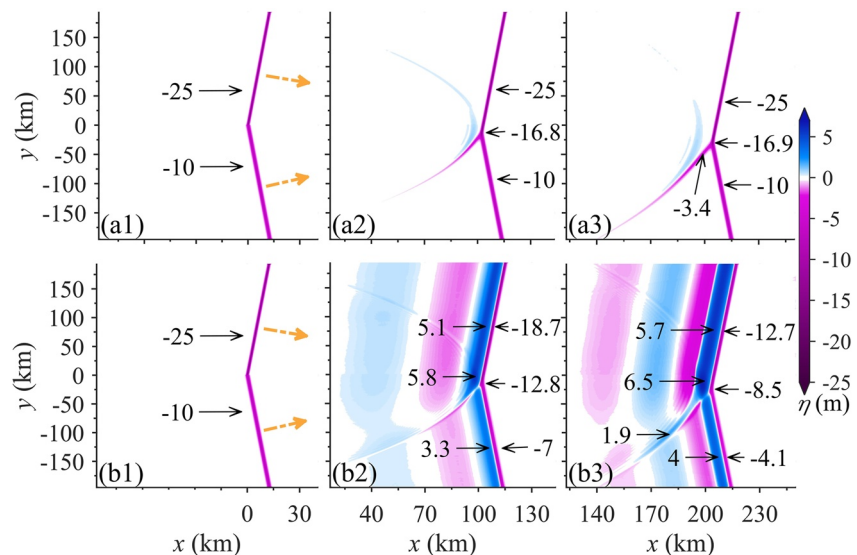

Figure 16. Experiment 3 with uniform depth 500 m and inclination angle $\psi_0 = 3.67°$. Panels (a1–a3) are selected to exhibit the evolution of wave amplitudes when rotation and shoaling topography are absent at time $t = 0$, 16.6, and 33.2 hr, respectively. In contrast, panels (b1–b3) are for the cases with rotation parameter $f = 1.0 \times 10^{-4}$ s^{-1} (flat bottom), and the layout is same as the top row. To exhibit the wave patterns in detail, the amplitudes η in regions specified by black arrows and the propagation directions of initial waves indicated by yellow dashed arrows are emphasized, respectively.
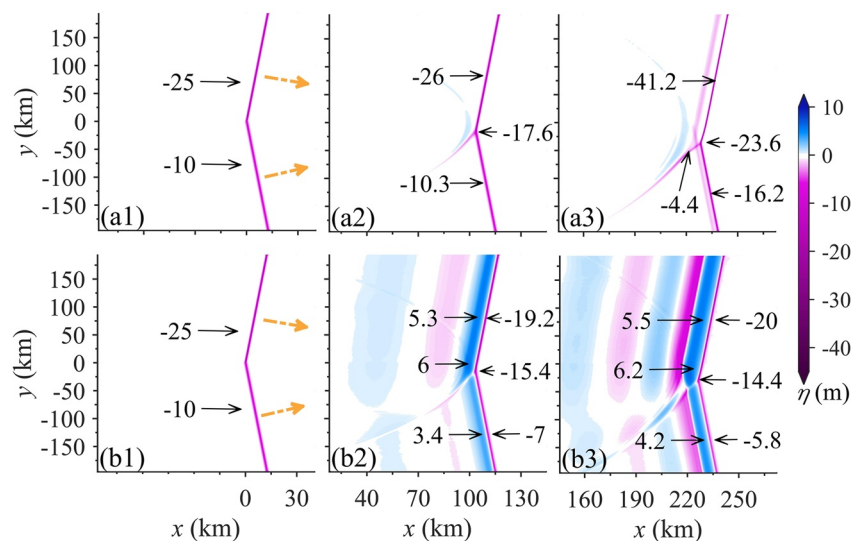
Figure 17. Experiment 3 with shoaling topography as shown in Figure 2. Panels (a1–a3) are selected to exhibit the evolution of wave amplitudes in the absence of rotation at time $t = 0$, 17.0, and 43.3 hr, respectively. In contrast, panels (b1–b3) are for the cases with rotation parameter $f = 1.0 \times 10^{-4}\,\text{s}^{-1}$ (shoaling topography is in presence), and the layout is same as the top row. To exhibit the wave patterns in detail, the amplitudes η in regions specified by black arrows and the propagation directions of initial waves indicated by yellow dashed arrows are emphasized, respectively.

for the theoretical asymptotic limit of the third wave. Due to the discrepancy in the propagation speed of the two initial wave branches (here, the upper branch is larger), the interaction point moves downward linearly with time. In addition, a small trailing wave with opposite polarity arises in the rear of the leading waves.

The inclusion of rotation ($f = 1.0 \times 10^{-4}\,\text{s}^{-1}$) renders some distortions on the wave evolution patterns resembling those in Experiments 1–2; see panels (b1–b3) in Figure 16. Nonetheless, the disparities of amplitudes between the upper and lower branch are diminished by the rotational effect (15 m vs. 8 m), which leads to the interaction point moving downward more slowly. The nascent third wave possesses a small amplitude and is susceptible to disintegration led by rotation; thus, in the ocean, this wave branch may be hardly visible. The magnitude of the rotation f impacts the evolution at different levels akin to those in the other two experiments (results not shown).

3.6. Experiment 3: Combined Effect of Rotation and Topography

The topographic effect alone is considered on the oblique ISW wave-wave interactions, which manifests as an augmentation of wave amplitudes and the emergence of two categories of trailing waves with the same and opposite polarities, respectively (Figure 17a3). Nevertheless, when the combined effect of rotation and topography is investigated, the evolution scenarios are similar to those in Experiments 1–2, especially the appearance of new wave packets as in Experiment 2, see panels (a1–a3) in Figure 18. Again, the competition between topographic and rotational effects plays a vital role in oblique ISW wave-wave interactions.

4. Discussions and Conclusions

Oblique ISW wave-wave interactions have received little attention in fluid dynamics and physical oceanography, despite that many aerial photographs and satellite images illustrating their ubiquities in oceans (see Chen et al., 2011; Wang & Pawlowicz, 2012; Xue et al., 2014 for instance). Furthermore, previous studies put much effort into comparisons with the theory by Miles (1977b); however, the results are not wholly satisfactory. The reason was attributed to the limitations of Miles theory by Shimizu and Nakayama (2017), and they suggested the use of an extended theory developed in Li et al. (2011); Kodama and Yeh (2016). Note that most of the studies have been based on images of surface signatures. It is very difficult to use in situ observational data to conduct research on this 3D phenomenon due to the need for high spatial and temporal coverage on underwater measurements, albeit we note Wang and Pawlowicz (2012) used single-point observational T/S and current profiles to supplement the image utilization. Another way to investigate this problem is to resort to numerical simulations;
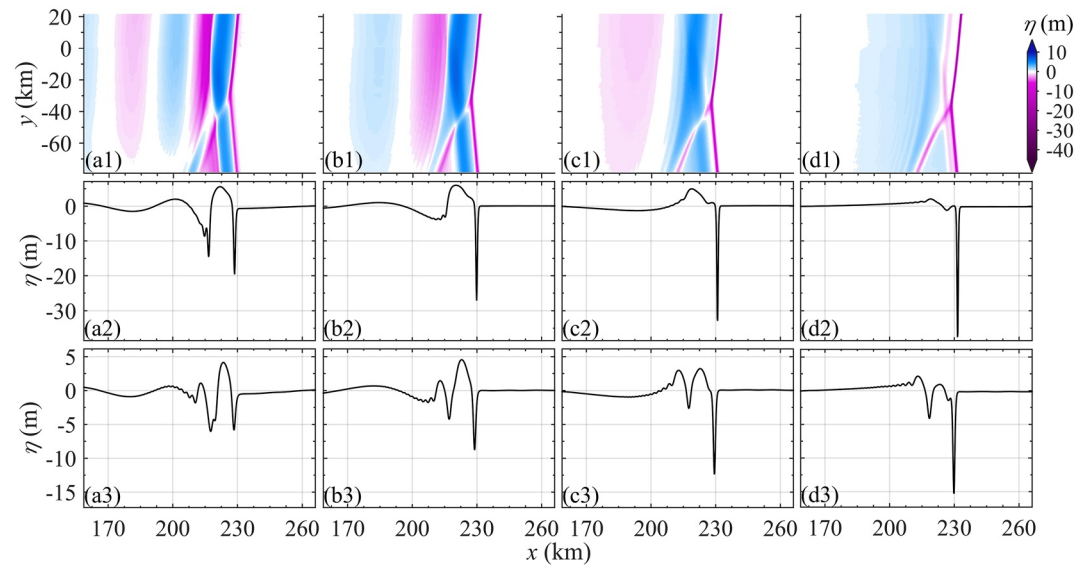
Figure 18. The top row is the horizontal view of wave amplitude for Experiment 3 under the circumstance of shoaling topography and rotation parameters $f = 1.0 \times 10^{-4}$, 7.5×10^{-5}, 5.0×10^{-5}, 2.5×10^{-5} s^{-1} in panels (a1–d1), respectively. The corresponding amplitudes along $y = 40$ km and $y = 0$ are exhibited in the second row (a2–d2) and the third row (a3–d3), respectively. The shoaling topography is shown in Figure 2, and the time is at $t = 43.3$ hr.

one of the rare studies is Shimizu and Nakayama (2017), in which they examined the oblique ISW wave-wave interactions in the Andaman Sea with the MITgcm model and the extended Miles theory. They discussed the emergence of stem-like waves and the inhibition of these waves induced by the Earth's rotation. Nevertheless, the magnitude of rotation they considered is relatively weak, and the topographic effect has a minor influence in their study as it occurred in water with depth ∼2,300 m at latitude 9°N.

In the ocean, some oblique ISW wave-wave interactions arise during the propagation up the continental slope/ shelf, such as the scenarios around Dongsha Atoll in the South China Sea, see Figure 1 in Yuan, Grimshaw, Johnson, and Wang (2018) and the collections of internal solitary waves in the World's oceans by Jackson (2004), in which the shoaling topography is supposed to have significant effects. Indeed, Yuan, Grimshaw, Johnson, and Wang (2018) used the variable-coefficient KP equation to examine the topographic effect on wave-wave interactions of an initial V-shaped wave. They illustrated six types of potential evolution regimes and chose three frequently recorded categories to exhibit the significance of varying topography. More recently, Yuan and Wang (2022) derived and utilized the bi-directional isotropic modified Benney-Luke equation, contrasting the uni-directional propagation and anisotropy of the KP equation, for the interactions between X-shaped internal solitary waves and the importance of shoaling topography was accentuated again.

While the deformation and the evolution regime shift due to shoaling of oblique ISW wave-wave interactions have been seldom studied, and the Earth's background rotational effect on the wave-wave interactions in a uniform environment has been rarely documented, especially for middle and high latitudes, their combined effects have not previously been examined in detail. This is the aim of this paper, and we have approached this task from a perspective of wave dynamics in the KP equation by designing experiments to check the evolution of initial V-shaped waves with/without shoaling topography under the circumstance of the Earth's rotation at the respective latitudes $\varphi = 0°$, $9.9°$, $20.1°$, $30.9°$, $43.3°$N. Generally speaking, the shoaling topography augments the leading wave amplitudes and renders trailing waves, whereas rotation disintegrates the coherent solitary wave into wave packets manifested as the decrease of leading wave amplitudes and the emergence of trailing waves. The competition between these two factors imposes more effects on the interaction zones than regions far away from the interaction zone and further, leads to disparate wave patterns.

In Experiment 1 (amplitudes $\eta_1 = \eta_2 = -15$ m and inclination angle $\psi_0 = 16°$), when shoaling topography is considered, a Mach stem arises in the interaction zone, which, however, does not appear when rotation is included ($f = 1.0 \times 10^{-4}$ s^{-1}, latitude $\varphi = 43.3°$N). Smaller rotation parameters f modulate the evolution to a less extent, and when $f < 7.5 \times 10^{-5}$ s^{-1}, the Mach stem emerges again, despite it being weakened by rotation, which coincides

with the findings in Shimizu and Nakayama (2017). In Experiment 2 (amplitudes $\eta_1 = \eta_2 = -20$ m and inclination angle $\psi_0 = 8°$), the combination of initial wave amplitudes and inclination angle intrinsically determines a robust wave resonance, in which even the relatively large rotation $f = 1.0 \times 10^{-4}$ s^{-1} can only impede the development of the amplitude and length of the Mach stem, but can not prevent its emergence. When the shoaling topography is incorporated, it magnifies the wave amplitude and causes a nascent wavepacket akin to the early stage of a KdV-like undular bore as found in Grimshaw et al. (2014). Remarkably, this emergence of a undular bore is closely related to the competition of shoaling topography and rotation, and smaller parameters f fail to generate this wavepacket. In Experiment 3 (amplitudes $\eta_1 = -25$ m, $\eta_2 = -10$ m and inclination angle $\psi_0 = 3.67°$), the scenarios with the combined effect of topography and rotation are generally similar to the previous two experiments, except that the interaction point moves downward due to different propagation speeds of the two branches. Another notable characteristic is that topography and rotation jointly deform the wave patterns and make the small-amplitude post-interaction waves nearly invisible, which presumably indicates the discrepancies between previous theoretical results in the absence of this combined effect and the recorded waves in the ocean, see our Figure 1 and the figures in Chen et al. (2011); Shimizu and Nakayama (2017) for example,

This study suggests the potential significance of oblique ISW wave-wave interactions in the ocean, given that the realistic continuous stratification and Earth's rotation are used here. Note that Mach stem seems able to occur frequently and to be robust for the appropriate combination of amplitudes and inclination angle of two initial waves in the environmental fluid. More importantly, the well-known fourfold enhancement of the Mach stem amplitude can be intensified by the combined effect of rotation and shoaling topography, which renders large amplitude and strong shear, thereby leading to wave-breaking events and may have consequences to ocean mixing, sediment transportation, and offshore engineering (Boegman & Stastna, 2019; Whalen et al., 2020).

Finally, it is necessary to adumbrate other physical factors which are worth further investigation. Due to the assumptions of the KP equation, the transformation between mode-1 and mode-2 ISWs is essentially excluded in this paper, but, at specific situations, it is important for wave dynamics (Terletska et al., 2016; Yang et al., 2009; Yuan et al., 2018). Essentially, the KP equation is a weakly nonlinear equation, lacking of the capacity to describe large-amplitude waves, although some studies (see Ostrovsky and Stepanyants (2005); Li et al. (2015) for instance) exhibited that it is also valid for relatively large amplitudes. The KP equation requires that variations in the transverse direction (here y) are one-order of magnitude smaller than those in the propagation direction (here x), indicating a potential failure for large inclination angles. Nevertheless, Yuan and Wang (2022) made comparisons with an isotropic (then no prescribed restrictions on inclination angles) equation for ISW wave-wave interactions, which illustrated that the KP equation is still valid when the angle is as large as 33° (much larger than the angles used in this paper). Background current are not considered in this paper, but they may considerably impact wave evolution for some cases (Lamb, 2010; Zhang, Xu, et al., 2018; Zhang, Huang, et al., 2018). To fully understand the dynamics, here the idealized shoaling topography varies along only one direction, while in the ocean, the variations of topography are complex (including undersea ridges, canyons, and plateau, etc.), as shown in Xie et al. (2019), even small bumpy features pose a perceptible modulation on wave dynamics. In addition, bottom friction becomes important when internal waves propagate into the shallow water and it can decrease the wave amplitude and affect the turbulent production (Henderson, 2016; Tan et al., 2019), whose impacts on the ISW wave-wave interactions are unclear.

Data Availability Statement

Figures were made with Matplotlib version 3.5.2 (Caswell et al., 2022), available under the Matplotlib license at https://matplotlib.org/. The computer codes used to perform data analyses are available in Yuan (2023).

References

Boegman, L., & Stastna, M. (2019). Sediment resuspension and transport by internal solitary waves. *Annual Review of Fluid Mechanics*, *51*(1), 129–154. https://doi.org/10.1146/annurev-fluid-122316-045049

Cai, S., & Xie, J. (2010). A propagation model for the internal solitary waves in the northern South China Sea. *Journal of Geophysical Research*, *115*(C12), C12074. https://doi.org/10.1029/2010JC006341

Caswell, T., Droettboom, M., Lee, A., De Andrade, E., Hoffmann, T., Klymak, J., & Ivanov, P. (2022). Matplotlib v3.5.2. [Software]. Zenodo. https://doi.org/10.5281/zenodo.6513224

Chakravarty, S., & Kodama, Y. (2009). Soliton solutions of the KP equation and application to shallow water waves. *Studies in Applied Mathematics*, *123*(1), 83–151. https://doi.org/10.1111/j.1467-9590.2009.00448.x

Chakravarty, S., & Kodama, Y. (2008). Classification of the line-soliton solutions of KPII. *Journal of Physics A: Mathematical and Theoretical*, *41*(27), 275209. https://doi.org/10.1088/1751-8113/41/27/275209

Chakravarty, S., & Kodama, Y. (2013). Construction of KP solitons from wave patterns. *Journal of Physics A: Mathematical and Theoretical*, *47*(2), 025201. https://doi.org/10.1088/1751-8113/47/2/025201

Chao, S.-Y., Shaw, P.-T., Hsu, M.-K., & Yang, Y.-J. (2006). Reflection and diffraction of internal solitary waves by a circular island. *Journal of Oceanography*, *62*(6), 811–823. https://doi.org/10.1007/s10872-006-0100-4

Chen, G., Liu, C., Wang, Y., & Hsu, M. (2011). Interaction and generation of long-crested internal solitary waves in the South China Sea. *Journal of Geophysical Research*, *116*(C6), C06013. https://doi.org/10.1029/2010JC006392

Chen, Y., & Yeh, H. (2014). Laboratory experiments on counter-propagating collisions of solitary waves. Part 1. Wave interactions. *Journal of Fluid Mechanics*, *749*, 577–596. https://doi.org/10.1017/jfm.2014.231

Deng, X., & Cai, S. (2017). A numerical study of rotation effect on the propagation of nonlinear internal solitary waves in the northern South China Sea. *Applied Mathematical Modelling*, *46*, 581–590. https://doi.org/10.1016/j.apm.2017.01.085

Farmer, D., Li, Q., & Park, J. (2009). Internal wave observations in the South China Sea: The role of rotation and non-linearity. *Atmosphere-Ocean*, *47*(4), 267–280. https://doi.org/10.3137/OC313.2009

Gilman, O. A., Grimshaw, R., & Stepanyants, Y. A. (1996). Dynamics of internal solitary waves in a rotating fluid. *Dynamics of Atmospheres and Oceans*, *23*(1–4), 403–411. https://doi.org/10.1016/0377-0265(95)00426-2

Grimshaw, R. (1981). Evolution equations for long nonlinear internal waves in stratified shear flows. *Studies in Applied Mathematics*, *65*(2), 159–188. https://doi.org/10.1002/sapm1981652159

Grimshaw, R. (1985). Evolution equations for weakly nonlinear, long internal waves in a rotating fluid. *Studies in Applied Mathematics*, *73*(1), 1–33. https://doi.org/10.1002/sapm19857311

Grimshaw, R., da Silva, J., & Magalhaes, J. M. (2017). Modelling and observations of oceanic nonlinear internal wave packets affected by the Earth's rotation. *Ocean Modelling*, *116*, 146–158. https://doi.org/10.1016/j.ocemod.2017.06.009

Grimshaw, R., Guo, C., Helfrich, K., & Vlasenko, V. (2014). Combined effect of rotation and topography on shoaling oceanic internal solitary waves. *Journal of Physical Oceanography*, *44*(4), 1116–1132. https://doi.org/10.1175/JPO-D-13-0194.1

Grimshaw, R., He, J. M., & Ostrovsky, L. A. (1998). Terminal damping of a solitary wave due to radiation in rotational systems. *Studies in Applied Mathematics*, *101*(2), 197–210. https://doi.org/10.1111/1467-9590.00090

Grimshaw, R., & Helfrich, K. (2008). Long-time solutions of the Ostrovsky equation. *Studies in Applied Mathematics*, *121*(1), 71–88. https://doi.org/10.1111/j.1467-9590.2008.00412.x

Grimshaw, R., & Helfrich, K. (2012). The effect of rotation on internal solitary waves. *IMA Journal of Applied Mathematics*, *77*(3), 326–339. https://doi.org/10.1093/imamat/hxs024

Grimshaw, R., Helfrich, K., & Johnson, E. (2013). Experimental study of the effect of rotation on nonlinear internal waves. *Physics of Fluids*, *25*(5), 056602. https://doi.org/10.1063/1.4805092

Guo, C., & Chen, X. (2014). A review of internal solitary wave dynamics in the northern South China Sea. *Progress in Oceanography*, *121*, 7–23. https://doi.org/10.1016/j.pocean.2013.04.002

Helfrich, K. (2007). Decay and return of internal solitary waves with rotation. *Physics of Fluids*, *19*(2), 293–128. https://doi.org/10.1063/1.2472509

Helfrich, K., & Ostrovsky, L. A. (2022). Effects of rotation and topography on internal solitary waves governed by the rotating Gardner equation. *Nonlinear Processes in Geophysics*, *29*(2), 207–218. https://doi.org/10.5194/npg-29-207-2022

Henderson, S. M. (2016). Turbulent production in an internal wave bottom boundary layer maintained by a vertically propagating seiche. *Journal of Geophysical Research: Oceans*, *121*(4), 2481–2498. https://doi.org/10.1002/2015JC011071

Jackson, C. R. (2004). *An atlas of internal solitary-like waves and their properties*, 2nd ed. (Technical Report). Global Ocean Association. Retrieved from http://www.internalwaveatlas.com

Kadomtsev, B. B., & Petviashvili, V. I. (1970). On the stability of solitary waves in weakly dispersing media. *Soviet Physics - Doklady*, *15*, 539–541.

Kodama, Y. (2010). KP solitons in shallow water. *Journal of Physics A: Mathematical and Theoretical*, *43*(43), 434004. https://doi.org/10.1088/1751-8113/43/43/434004

Kodama, Y., & Yeh, H. (2016). The KP theory and Mach reflection. *Journal of Fluid Mechanics*, *800*, 766–786. https://doi.org/10.1017/jfm.2016.422

Lamb, K. G. (2010). Energetics of internal solitary waves in a background sheared current. *Nonlinear Processes in Geophysics*, *17*(5), 553–568. https://doi.org/10.5194/npg-17-553-2010

Li, L., Wang, C., & Grimshaw, R. (2015). Observation of internal wave polarity conversion generated by a rising tide. *Geophysical Research Letters*, *42*(10), 4007–4013. https://doi.org/10.1002/2015GL063870

Li, Q., & Farmer, D. (2011). The generation and evolution of nonlinear internal waves in the deep basin of the South China Sea. *Journal of Physical Oceanography*, *41*(7), 1345–1363. https://doi.org/10.1175/2011JPO4587.1

Li, W., Yeh, H., & Kodama, Y. (2011). On the Mach reflection of a solitary wave: Revisited. *Journal of Fluid Mechanics*, *672*, 326–357. https://doi.org/10.1017/S0022112010006014

Maderich, V., Jung, K. T., Terletska, K., & Kim, K. O. (2017). Head-on collision of internal waves with trapped cores. *Nonlinear Processes in Geophysics*, *24*(4), 751–762. https://doi.org/10.5194/npg-24-751-2017

Miles, J. W. (1977a). Obliquely interacting solitary waves. *Journal of Fluid Mechanics*, *79*(1), 157–169. https://doi.org/10.1017/S0022112077000081

Miles, J. W. (1977b). Resonantly interacting solitary waves. *Journal of Fluid Mechanics*, *79*(1), 171–179. https://doi.org/10.1017/S0022112077000093

Mirie, R. M., & Su, C. H. (1984). Internal solitary waves and their head-on collision. Part 1. *Journal of Fluid Mechanics*, *147*(-1), 213–231. https://doi.org/10.1017/S0022112084002068

Ostrovsky, L. A. (1978). Nonlinear internal waves in a rotating ocean (in Russian). *Oceanology*, *18*(2), 119. https://doi.org/10.1016/0302-184X(78)90008-2

Ostrovsky, L. A., & Stepanyants, Y. A. (2005). Internal solitons in laboratory experiments: Comparison with theoretical models. *Chaos*, *15*(3), 037111. https://doi.org/10.1063/1.2107087

Ramp, S. R., Yang, Y.-J., Jan, S., Chang, M.-H., Davis, K. A., Sinnett, G., et al. (2022). Solitary waves impinging on an isolated tropical reef: Arrival patterns and wave transformation under shoaling. *Journal of Geophysical Research: Oceans*, *127*(3), e2021JC017781. https://doi.org/10.1029/2021JC017781

Schlatter, P., Adams, N. A., & Kleiser, L. (2005). A windowing method for periodic inflow/outflow boundary treatment of non-periodic flows. *Journal of Computational Physics*, *206*(2), 505–535. https://doi.org/10.1016/j.jcp.2004.12.015

Shimizu, K., & Nakayama, K. (2017). Effects of topography and Earth's rotation on the oblique interaction of internal solitary-like waves in the Andaman Sea. *Journal of Geophysical Research: Oceans*, *122*(9), 7449–7465. https://doi.org/10.1002/2017JC012888

Su, C. H., & Mirie, R. M. (1980). On head-on collisions between two solitary waves. *Journal of Fluid Mechanics*, *98*(3), 509–525. https://doi.org/10.1017/S0022112080000262

Tan, D., Zhou, J., Wang, X., & Wang, Z. (2019). Combined effects of topography and bottom friction on shoaling internal solitary waves in the South China Sea. *Applied Mathematics and Mechanics*, *40*(4), 421–434. https://doi.org/10.1007/s10483-019-2465-8

Terletska, K., Jung, K. T., Talipova, T., Maderich, V., Brovchenko, I., & Grimshaw, R. (2016). Internal breather-like wave generation by the second mode solitary wave interaction with a step. *Physics of Fluids*, *28*(11), 116602. https://doi.org/10.1063/1.4967203

Vlasenko, V., Stashchuk, N., Guo, C., & Chen, X. (2010). Multimodal structure of baroclinic tides in the South China Sea. *Nonlinear Processes in Geophysics*, *17*(5), 529–543. https://doi.org/10.5194/npg-17-529-2010

Wang, C., & Pawlowicz, R. (2012). Oblique wave-wave interactions of nonlinear near-surface internal waves in the Strait of Georgia. *Journal of Geophysical Research*, *117*(C6), C06031. https://doi.org/10.1029/2012jc008022

Whalen, C. B., de Lavergne, C., Garabato, A. C. N., Klymak, J. M., MacKinnon, J. A., & Sheen, K. L. (2020). Internal wave-driven mixing: Governing processes and consequences for climate. *Nature Reviews Earth & Environment*, *1*(11), 606–621. https://doi.org/10.1038/s43017-020-0097-z

Xie, J., He, Y., & Cai, S. (2019). Bumpy topographic effects on the transbasin evolution of large-amplitude internal solitary wave in the northern South China Sea. *Journal of Geophysical Research: Oceans*, *124*(7), 4677–4695. https://doi.org/10.1029/2018JC014837

Xue, J., Graber, H. C., Romeiser, R., & Lund, B. (2014). Understanding internal wave–wave interaction patterns observed in satellite images of the Mid-Atlantic Bight. *IEEE Transactions on Geoscience and Remote Sensing*, *52*(6), 3211–3219. https://doi.org/10.1109/TGRS.2013.2271777

Yang, Y. J., Fang, Y. C., Chang, M. H., Ramp, S. R., Kao, C. C., & Tang, T. Y. (2009). Observations of second baroclinic mode internal solitary waves on the continental slope of the northern South China Sea. *Journal of Geophysical Research*, *114*(C10), 1–15. https://doi.org/10.1029/2009JC005318

Yeh, H., Li, W., & Kodama, Y. (2010). Mach reflection and KP solitons in shallow water. *The European Physical Journal*, *185*(1), 97–111. https://doi.org/10.1140/epjst/e2010-01241-0

Yuan, C. (2023). Code for the oblique internal solitary wave-wave interactions. [Software]. Zenodo. https://doi.org/10.5281/zenodo.7820044

Yuan, C., Grimshaw, R., & Johnson, E. (2018). The evolution of second mode internal solitary waves over variable topography. *Journal of Fluid Mechanics*, *836*, 238–259. https://doi.org/10.1017/jfm.2017.812

Yuan, C., Grimshaw, R., Johnson, E., & Chen, X. (2018). The propagation of internal solitary waves over variable topography in a horizontally two-dimensional framework. *Journal of Physical Oceanography*, *48*(2), 283–300. https://doi.org/10.1175/JPO-D-17-0154.1

Yuan, C., Grimshaw, R., Johnson, E., & Wang, Z. (2018). Topographic effect on oblique internal wave-wave interactions. *Journal of Fluid Mechanics*, *856*, 36–60. https://doi.org/10.1017/jfm.2018.678

Yuan, C., Grimshaw, R., Johnson, E., & Whitfield, A. (2020). Generation of nonlinear internal waves by flow over topography: Rotational effects. *Physical Review E*, *101*(3), 033104. https://doi.org/10.1103/PhysRevE.101.033104

Yuan, C., & Wang, Z. (2022). On diffraction and oblique interactions of horizontally two-dimensional internal solitary waves. *Journal of Fluid Mechanics*, *936*, A20. https://doi.org/10.1017/jfm.2022.60

Zhang, P., Xu, Z., Li, Q., Yin, B., Hou, Y., & Liu, A. K. (2018). The evolution of mode-2 internal solitary waves modulated by background shear currents. *Nonlinear Processes in Geophysics*, *25*(2), 441–455. https://doi.org/10.5194/npg-25-441-2018

Zhang, X., Huang, X., Zhang, Z., Zhou, C., Tian, J., & Zhao, W. (2018). Polarity variations of internal solitary waves over the continental shelf of the northern South China Sea: Impacts of seasonal stratification, mesoscale eddies, and internal tides. *Journal of Physical Oceanography*, *48*(6), 1349–1365. https://doi.org/10.1175/JPO-D-17-0069.1

Zhang, Z., Fringer, O. B., & Ramp, S. R. (2011). Three-dimensional, nonhydrostatic numerical simulation of nonlinear internal wave generation and propagation in the South China Sea. *Journal of Geophysical Research*, *116*(C5), C05022. https://doi.org/10.1029/2010JC006424

Zou, L., Li, Y., Hu, Y., Wang, Z., & Yu, Z. (2020). Frontal collision of two nonlinear internal solitary waves in a stratified fluid. *Applied Ocean Research*, *104*, 102334. https://doi.org/10.1016/j.apor.2020.102334